Fluid-structure interaction dynamics and feedback control of multiple flexible bioinspired swimmers

Rose Gebhardt
Dept. of Aerospace Engineering
University of Maryland
College Park, MD
rgebhard@umd.edu

Haotian Hang
Dept. of Aerospace and Mechanical Engineering
University of Southern California
Los Angeles, CA
haotianh@usc.edu

Derek A. Paley
Dept. of Aerospace Engineering
Institute for Systems Research
University of Maryland
College Park, MD
dpaley@umd.edu

Eva Kanso
Dept. of Aerospace and Mechanical Engineering
University of Southern California
Los Angeles, CA
kanso@usc.edu

***Abstract*—Fish swim by bending their bodies as fluid–structure interactions occur between elastic tissues and the surrounding flow, yet modeling many such swimmers with near-body hydrodynamics is computationally difficult. This paper presents a modeling framework for multiple flexible fish with near-body hydrodynamic interactions and a low computational cost. We model each elastic fish body using Bergou's theory of elastic rods constrained to planar movement. We use a vortex sheet method to model the flow around each fish and the wake created by its motion. We introduce a control law to highlight the utility of this platform for control design and evaluation. All components of the model are integrated to simulate several schooling patterns. This approach provides a practical testbed for studying flow-mediated coordination, exploring design rules for energy-efficient collectives, and rapidly prototyping control strategies for bioinspired robotic schools.**

***Index Terms*—bioinspired engineering, elasticity, fluid structure interactions, numerical simulation**

I. Introduction

The propulsion methods of bioinspired robotic fish have been extensively studied for their potential to achieve higher efficiency than traditional propeller-driven autonomous underwater vehicles [1], [2]. In particular, schooling robotic fish can take advantage of the vortices shed by nearby agents, leading to enhanced propulsive performance and enabling environmental monitoring through distributed sensing [3]–[7]. Furthermore, body flexibility has been identified as a key factor in both thrust generation and maneuverability [8]–[10].

Building on these ideas, we aim to study the interactions between flexible fish in schools by developing a dynamic model of a fish based on Bergou's theory of elastic rods. The discrete geometric model of thin, flexible rods introduced by Bergou *et al.* provides a framework for describing the configuration and dynamics of centerline deformations in slender rods [11], [12]. This model has since been applied to study the behavior of soft robotic systems. A caterpillar-inspired soft robot was modeled using Bergou's theory constrained to planar movement, which the authors refer to as the discrete planar elastic rod (DPER) framework [13]. DPER has also been used to model the locomotion of swimming snakes and eels by incorporating the effects of fluid-structure interactions through drag and added mass forces [14], [15].

To incorporate the effect of the shedded vortices, we applied the inviscid vortex sheet method (VSM), which is suited for capturing hydrodynamic effects at intermediate Reynolds numbers (Re $\sim 10^3 - 10^5$) [16]. This method has been adapted for application to flexible one-dimensional sheets and used to study flow interactions in fish and birds in the flow regime [7], [10], [17]–[21]. We apply VSM to a two-dimensional flexible fish model to simulate interactions between multiple agents, capturing near-body hydrodynamic effects with low computational cost.

The specific contributions of this paper are (1) a description of the configuration of a discretized elastic fish body and a derivation of the internal restorative forces it experiences; (2) a detailed model of the flow field, capturing the influence of the body on the flow, the wakes generated by each fish, and the resulting fluid–structure interactions; and (3) and a controller design that uses both feedback and feedforward control to steer each fish to a desired heading. These are all integrated to construct a simulation framework enabling the study of flexible fish-to-fish interactions with relatively low computational cost.

The outline of this paper is as follows. Section II presents a model of planar elastic rods and the resultant internal forces and applies this framework to simulate a self-propelling flexible fish body. Section III describes the vortex sheet method used to simulate the surrounding fluid flow and the resulting external hydrodynamic forces acting on each fish. Section IV introduces feedback control and integrates all components of the model to simulate interactions among multiple flexible fish swimming in a school. Section V summarizes the key findings and discusses ongoing and future work.

II. Flexible Body Model

We model the internal elastic forces on a fish based on Bergou's description of a discrete elastic rod restricted to a planar configuration [11]. This model provides the restorative

This work was made possible by funding from the Office of Naval Research under Grant Number N000142212655.

stretching and bending forces that arise when the fish deviates from its reference configuration. This section describes Bergou's theory, adapts it to represent a deformable fish, and presents the resultant internal forces on the fish.

A. Discrete Planar Elastic Rod Definition

Consider a continuous rod, $F = \{f(s); \hat{\mathbf{t}}(s), \hat{\mathbf{n}}(s)\}$, where $f(s)$ is the curve parameterized by arc length s in $\mathbb{R}^2$, $\hat{\mathbf{t}}(s) = \frac{\partial f}{\partial s}$ is the parameterized tangent vector, and $\hat{\mathbf{n}}(s) = E_3 \times \hat{\mathbf{t}}(s)$ is the parameterized normal vector. From these values, we then define $\kappa(s) = \frac{\partial \hat{\mathbf{t}}(s)}{\partial s}$ as the curvature normal vector [11].

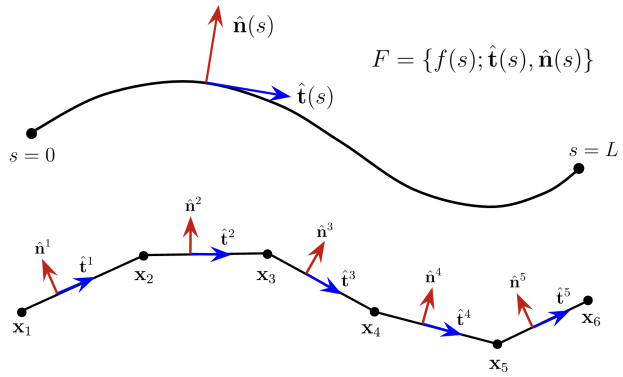

Fig. 1: Schematic of a continuous planar elastic rod (top) and its corresponding discretized representation (bottom), along with their respective configuration values.

In the continuous planar case, the total elastic energy comes from the bending energy [11],

$$E_{bend}(F) = \frac{1}{2}\int_{s=0}^{L} \alpha(s)(\kappa - \bar{\kappa})^2 \mathrm{d}s, \tag{1}$$

where $\alpha(s)$ is the bending modulus along the rod and $\bar{\kappa}$ is the natural curvature along the rod.

Using the same ideas behind the continuous elastic rod formulation, we proceed to define a discretized elastic rod, as represented in Figure 1. Throughout this description, values associated with discretized nodes are denoted using subscripts, $(\cdot)_k$, whereas values associated with resultant edges are denoted using superscripts, $(\cdot)^k$.

The curve $f(s)$ is discretized into N nodes, denoted $\{\mathbf{x}_k\}_{k=1}^{N}$, and $N-1$ edges, $\{\mathbf{e}^k\}_{k=1}^{N-1}$, where each edge is defined as $\mathbf{e}^k = \mathbf{x}_{k+1} - \mathbf{x}_k$. The length of edge k is given by $l^k = \|\mathbf{e}^k\|$, and the turning angle between adjacent edges is denoted by ϕ_k. The discrete tangent vector along edge k is the unit direction vector $\hat{\mathbf{t}}^k = \frac{\mathbf{e}^k}{\|\mathbf{e}^k\|}$, and the corresponding discrete normal vector is defined as $\hat{\mathbf{n}}^k = E_3 \times \hat{\mathbf{t}}^k$, consistent with the continuous case.

We define the curvature at each node in terms of the radius of the osculating circle, as illustrated in Figure 2. This circle is constructed to be tangent to the curve at two points located a distance of $\frac{l_k}{2}$ from the node $\mathbf{x}_k$ along the adjacent edges, where l_k is the Voronoi length associated with the node, given by $l_k = \frac{1}{2}(l^{k-1} + l^k)$. Based on this geometric construction, the radius of the osculating

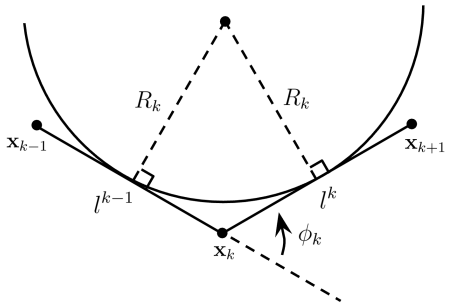

Fig. 2: Schematic of an osculating circle used to define discretized curvature.

circle is given by $R_k = \frac{1}{2} l_k \cot(\frac{\phi_k}{2})$, and the curvature is $\hat{\kappa}_k = 1/R = 2\tan(\phi_k/2)/l_k$. Following convention in prior literature, quantities will be expressed in terms of the integrated curvature, defined as [11]

$$\kappa_k = \hat{\kappa}_k l_k = 2\tan\left(\frac{\phi_k}{2}\right). \tag{2}$$

We can now define the discrete analog of the elastic bending energy from (1) using the summation over internal nodes [11]

$$E_{bend} = \frac{1}{2}\sum_{k=2}^{N-1} \alpha_k(\hat{\kappa}_k - \bar{\hat{\kappa}}_k)^2 l_k = \frac{1}{2}\sum_{k=2}^{N-1} \alpha_k \frac{(\kappa_k - \bar{\kappa}_k)^2}{l_k}$$

in terms of both regular and integrated discrete curvatures. In terms of physical parameters, the bending modulus α_k is equal to the Young's modulus, E, multiplied by the moment of inertia about the E_3-axis, I. Assume that the E is constant throughout the rod, but $I = I_k$ will vary depending on the geometry of each edge. Putting these variables together, the full bending energy is [12]

$$E_{bend} = \frac{1}{2}\sum_{k=2}^{N-1} EI_k \frac{(\kappa_k - \bar{\kappa}_k)^2}{l_k}. \tag{3}$$

The bending elastic energy is used to compute the bending forces within the rod. By the nature of parameterizing the rod by arc length s in the continuous case, we assume that the rod is inextensible and do not include a stretching energy. This can be enforced using an auxiliary constraint, but in our implementation, we add terms to represent deviations in natural length and define an elastic stretching energy.

Let $\bar{l}^k$ be the natural length of each edge and specify that l^k is the true length. The axial strain along each edge is $\epsilon^k = \frac{l^k - \bar{l}^k}{\bar{l}^k}$ and the stretching modulus is $\alpha_{s,k} = EA^k$, where A^k is the cross-sectional area of each edge. Using these quantities, the elastic stretching energy is expressed as $E_{stretch} = \frac{1}{2}\sum_{k=1}^{N-1} \alpha_{s,k}(\epsilon^k)^2 \bar{l}^k$, or equivalently [12],

$$E_{stretch} = \frac{1}{2}\sum_{k=1}^{N-1} EA^k \left(\frac{l^k}{\bar{l}^k} - 1\right)^2 \bar{l}^k. \tag{4}$$

By incorporating the elastic stretching energy, the total elastic energy of the rod becomes $E_{elastic} = E_{bend} + E_{stretch}$, which is used to compute the internal forces in the rod.

B. Internal Elastic Forces

The conservative elastic forces acting on the nodes are defined as the variation of the total elastic energy with respect to changes in node positions, $\mathbf{F}_k = -\mathrm{d}E_{elastic}/\mathrm{d}\mathbf{x}_k$. We decompose this force term into components that we can implement by considering bending and stretching forces separately, and then expanding each into partial derivatives that are more easily evaluated. For brevity, we refer to the bending and stretching energy terms as E_b and E_s, respectively, for the remainder of this section.

To begin, both the elastic bending and stretching forces can be characterized by how deviations in edge vectors influence the bending and stretching energies [13],

$$\mathbf{F}_{b,k} = -\frac{\mathrm{d}E_b}{\mathrm{d}\mathbf{x}_k} = \frac{\partial E_b}{\partial \mathbf{e}^k} - \frac{\partial E_b}{\partial \mathbf{e}^{k-1}}, \tag{5}$$

$$\mathbf{F}_{s,k} = -\frac{\mathrm{d}E_s}{\mathrm{d}\mathbf{x}_k} = \frac{\partial E_s}{\partial \mathbf{e}^k} - \frac{\partial E_s}{\partial \mathbf{e}^{k-1}}. \tag{6}$$

The bending force terms can be further broken down into their dependence on the curvature and turning angle at each node,

$$\frac{\partial E_b}{\partial \mathbf{e}^k} = \frac{\partial E_b}{\partial \kappa_k}\frac{\partial \kappa_k}{\partial \phi_k}\frac{\partial \phi_k}{\partial \mathbf{e}^k} + \frac{\partial E_b}{\partial \kappa_{k+1}}\frac{\partial \kappa_{k+1}}{\partial \phi_{k+1}}\frac{\partial \phi_{k+1}}{\partial \mathbf{e}^k}.$$

Each partial derivative can be evaluated directly using previously established relationships and are as follows [13]

$$\frac{\partial E_b}{\partial \kappa_k} = \frac{EI_k(\kappa_k - \bar{\kappa}_k)}{2l_k}, \quad \frac{\partial \kappa_k}{\partial \phi_k} = \frac{2}{1+\cos\phi_k}$$
$$\frac{\partial \phi_k}{\partial \mathbf{e}^{k-1}} = -\frac{\hat{\mathbf{n}}^{k-1}}{l^{k-1}}, \quad \text{and} \quad \frac{\partial \phi_k}{\partial \mathbf{e}^k} = \frac{\hat{\mathbf{n}}^k}{l^k}$$

Similarly, the stretching force terms can be further broken down into their dependence on the edge length [13],

$$\frac{\partial E_s}{\partial \mathbf{e}^k} = \frac{\partial E_s}{\partial l^k}\frac{\partial l^k}{\partial \mathbf{e}^k} = EA^k\left(\frac{l^k}{\bar{l}^k} - 1\right)\hat{\mathbf{t}}^k.$$

The partial derivatives given are now sufficient to compute (5) and (6) based on the configuration of the rod.

Optionally, additional internal forces can arise from dissipative effects associated with bending and stretching. These are modeled as damping forces that cause the rod to lose elastic energy over time. Specifically, energy dissipation due to bending and stretching are assumed to be proportional to the rate of change of integrated curvature squared and the rate of change of edge length squared, respectively, i.e., [15]

$$\mathcal{F}_b = \frac{d_b}{2}\sum_{k=2}^{N-1}(\dot{\kappa_k})^2, \quad \mathbf{F}_{bd,k} = -\frac{\partial \mathcal{F}_b}{\partial \dot{\mathbf{x}}_k} \tag{7}$$

$$\mathcal{F}_s = \frac{d_s}{2}\sum_{k=1}^{N-1}(\dot{l^k})^2, \quad \mathbf{F}_{sd,k} = -\frac{\partial \mathcal{F}_s}{\partial \dot{\mathbf{x}}_k} \tag{8}$$

Dissipation functions and associated forces for bending and stretching are shown in (7) and (8), respectively. Implementation details are omitted for brevity; see [15].

C. Discretized Elastic Fish

We now use Bergou's elastic rod theory to model a swimming fish by defining a rod with physical parameters that capture a fish's shape and prescribing a time-varying natural curvature to simulate body deformations during motion.

The physical parameters of each link are based on a discretized Joukowski foil profile, as shown in Figure 3. This profile is commonly used to model the body shape and hydrodynamic behavior of carangiform swimmers [22], [23]. The centerline of the foil is divided into $N-1$ segments of equal length, l^k. The thickness of each segment, h^k, is the average of the thicknesses at its two endpoints, and the width of each segment, w^k is set to one quarter of the fish's length.

Fig. 3: Visualization of how a fish body is discretized.

These values are then used to define the cross-sectional area, mass, and moment of inertia of each segment as

$$A^k = \frac{\pi h^k w^k}{4}, \; m^k = \frac{\pi \rho l^k h^k w^k}{4}, \; \text{and} \; I^k = \frac{1}{12}m^k(w^k)^2,$$

where ρ is uniform density of the fish.

To simulate swimming motion, we prescribe time-varying natural turning angles along the body using a backward-propagating wave with an quadratic envelope,

$$\bar{\phi}_k(t, s_k) = A(c_1 s_k + c_2 s_k^2)\left(\sin(\beta s_k + \omega t + \varphi) + \phi_0\right), \tag{9}$$

where s_k is the distance of node k from the head along the centerline. The parameters β, ω, and φ define the wave number, angular frequency, and phase offset of the swimming motion, respectively; ϕ_0 is a bias term that is used as a steering input. The quadratic envelope amplifies tail movements relative to those of the head, which imitates the motion pattern of carangiform swimming [24]. From here, the natural turning angles are mapped to the natural integrated curvature according to (2).

III. Flow Field Model

The fluid-structure interaction is simulated in the context of the inviscid vortex sheet model [7], [10], [16]–[21], [25]. Each fish has an associated bound vortex sheet to model its impact on the surrounding flow, and as each fish swims, it sheds a free vortex sheet from its trailing edge that models its wake. Similar to the treatment of the fish body, we first formulate the vortex sheets in a continuous framework, then provide a detailed description of their discretization and implementation.

The bound vortex sheet is described by its position $\mathbf{x}_b(s,t)$ and strength $\gamma(s,t)$, where $s \in [0, L]$ is the curvilinear coordinate along the swimmer starting from its leading edge, consistent with Figures 1 and 4. The separated sheet is described by its position $\mathbf{x}_w(\Gamma, t)$, $\Gamma \in [0, \Gamma_w]$, where Γ is the Lagrangian circulation around the portion of the separated sheet between its free end in the spiral and the point $\mathbf{x}_w(\Gamma, t)$.

Each vortex sheet is defined using the vortex blob kernel with regularization parameter δ [10] at position $\mathbf{x} = (x, y)$,

$$\mathbf{K}_\delta(\mathbf{x}) = \frac{1}{2\pi} \frac{(-y, x)}{x^2 + y^2 + \delta^2}. \tag{10}$$

The free sheet is regularized using the vortex blob method to prevent the growth of the Kelvin-Helmholtz instability while the bound sheet is not regularized in order to preserve the invertibility of the map between the sheet strength and the normal velocity along the sheet. The velocity components induced by the bound and free vortex velocity components, $\mathbf{u}_b(\mathbf{x})$ and $\mathbf{u}_w(\mathbf{x})$, respectively, are [16]

$$\mathbf{u}_b(\mathbf{x}, t) = \int_0^L \mathbf{K}_0(\mathbf{x} - \mathbf{x}_b(s, t))\gamma(s, t)\mathrm{d}s \quad \text{and}$$

$$\mathbf{u}_w(\mathbf{x}, t) = \int_0^{\Gamma_w} \mathbf{K}_\delta(\mathbf{x} - \mathbf{x}_w(\Gamma, t))\mathrm{d}\Gamma.$$

The net flow velocity field is then composed of three potential flows: the prescribed external flow $\mathbf{u}_e(\mathbf{x})$, the contribution of the bound vortex sheets $\mathbf{u}_b(\mathbf{x})$, and the contribution of the free vortex sheets $\mathbf{u}_w(\mathbf{x})$. The net flow field can be found by superposition due to the linearity of the model, i.e, $\mathbf{u}(\mathbf{x}) = \mathbf{u}_e(\mathbf{x}) + \mathbf{u}_b(\mathbf{x}) + \mathbf{u}_w(\mathbf{x})$.

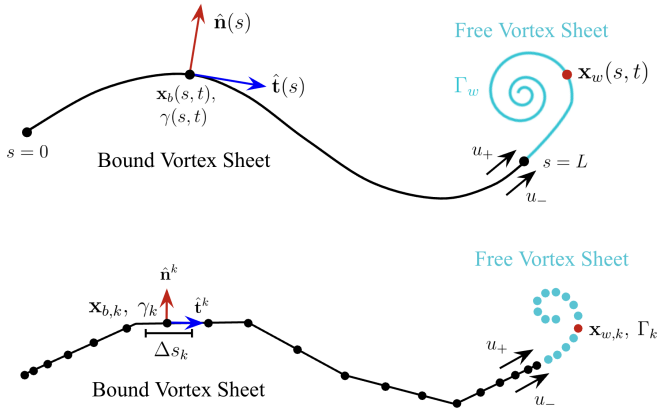

Fig. 4: Vortex sheet model applied to a two-dimensional flexible swimmer. Shown in both full continuous form on a smooth curved body (top) and in discretized form applied to a discretized bending body (bottom).

The details on how bound and free vortex sheets are constructed are laid out in the remainder of this section.

A. Bound Vortex Sheet

In the discretized formulation, bound vortex sheets are located at fixed Chebyshev points, $\mathbf{x}_{b,k}$, along the centerline of each fish [10]. These points are non-uniformly spaced and clustered most densely clustered at the two ends of the fish. Each bound vortex has strength $\gamma_k \Delta s_k$, where Δs_k is the Voronoi length associated with each node and strength γ_k is to be solved. The velocity contribution of the discretized bound vortex sheet is [10]

$$\mathbf{u}_b(\mathbf{x}) = \sum_{k=0}^{N_b} \gamma_k \Delta s_k \mathbf{K}_0(\mathbf{x} - \mathbf{x}_{b,k})$$

To solve the unknown bound vortex sheet strength, we introduce control points at the midpoints between bound vortices, $\mathbf{x}_b^k = \frac{1}{2}(\mathbf{x}_{b,k} + \mathbf{x}_{b,k+1})$. At these control points, we enforce the non-penetration condition which requires body velocity normal to the body surface to equal the flow normal to the body surface. Written out explicitly, this condition requires $\mathbf{u}(\mathbf{x}_b^k) \cdot \mathbf{n}^k = \dot{\mathbf{x}}_b^k \cdot \mathbf{n}^k$, or

$$\mathbf{u}_b(\mathbf{x}_b^k) \cdot \mathbf{n}^k = \dot{\mathbf{x}}_b^k \cdot \mathbf{n}^k - \mathbf{u}_w(\mathbf{x}_b^k) \cdot \mathbf{n}^k - \mathbf{u}_e(\mathbf{x}_b^k) \cdot \mathbf{n}^k \tag{11}$$

where only left hand contains unknowns γ_k. Note that $\dot{\mathbf{x}}_b^k$ is determined by the velocity of the fish.

This provides $N_b - 1$ constraints for each bound vortex sheet. The last constraint needed is the conservation of total circulation according to Kelvin's circulation theorem [10]. At the initial condition, there is zero net circulation and thus the net circulation will stay at zero, i.e,

$$\sum_{k=0}^{N_b} \gamma_k \Delta s_k + \sum_{k=0}^{N_w} \Gamma_k = 0, \tag{12}$$

where Γ_k are the discretized circulation strengths whose sum is Γ_w, as defined in the continuous formulation. The constraints provided in (11) and (12) give us all the information needed to compute the bound vortex sheet contribution.

B. Free Vortex Sheet

In the continuous form of the free sheet, the circulation parameter Γ along $\mathbf{x}_w(\Gamma, t)$ is determined by the shedding rate $\dot{\Gamma}_w$ according to the Kutta condition. This requires the pressure difference across the tail to be zero [16], or

$$[p_- - p_+]_{s=L} = \left[-\frac{d\Gamma}{dt} - \frac{1}{2}(u_-^2 - u_+^2)\right]_{s=L} = 0, \tag{13}$$

where u_- and u_+ are the tangential slip velocities at either side of the tail, defined by the equations evaluated at $s = L$,

$$\frac{(u_+ + u_-)}{2} = (\mathbf{u}(\mathbf{x}(s)) - \dot{\mathbf{x}}(s)) \cdot \hat{\mathbf{t}}(s), u_+ - u_- = \gamma(s). \tag{14}$$

This condition is fulfilled when the shedding rate is [16]

$$\dot{\Gamma}_w = -\frac{1}{2}\left(u_-^2 - u_+^2\right)^2 |_{s=L} \tag{15}$$

In implementation, the free vortex sheet is discretized into many individual point vortices. At each timestep, a new vortex sheds from the trailing edge of each swimmer. The strength of the new point vortex is the timestep duration, Δt, multiplied by the shedding rate $\dot{\Gamma}_w$, still defined by (15). Once a free vortex is shed, its velocity is equal to the flow velocity minus its own contribution. Each free vortex dissipates after time duration T_{diss}, at which point it is removed from the simulation.

C. Hydrodynamic Forces

With the flow field model defined, we now define the resulting hydrodynamic forces. We present a simplified closed-form model of the fluid dynamics, described in [14] and [15], for the sake of implementation runtime and for control-design purposes; more accurate but complex computation of the fluid forces are described in [25]. In this flow model, we find the

fluid drag and added mass forces on each elliptical cylinder link independently, and the resulting force components are then distributed across the connected nodes.

To compute the fluid drag forces, we use the tangential and normal drag coefficients, c_t^k and c_n^k, defined as [14]

$$c_t^k = \frac{1}{8}\rho_f \pi C_F l^k (h^k + w^k), \quad c_n^k = \frac{1}{2}\rho_f C_D l^k h^k,$$

where C_F and C_D are empirical drag coefficients based on the hydrodynamic response of an elliptical cylinder and ρ_f is the fluid density. We also use the relative velocities of each link in the tangential and normal directions, given by [14],

$$v_t^k = (\dot{\mathbf{x}}^k - \mathbf{u}(\mathbf{x}^k)) \cdot \hat{\mathbf{t}}^k, \quad v_n^k = (\dot{\mathbf{x}}^k - \mathbf{u}(\mathbf{x}^k)) \cdot \hat{\mathbf{n}}^k.$$

The drag is proportional to the relative velocity squared [1],

$$\mathbf{F}_D^k = -c_t^k \left(v_t^k |v_t^k|\right) \hat{\mathbf{t}}^k - c_n^k \left(v_n^k |v_n^k|\right) \hat{\mathbf{n}}^k. \tag{16}$$

The added mass term is linearly proportional to the acceleration of each link in the normal direction, scaled by an added mass coefficient $\mu_N^k = \frac{1}{4}\rho_f \pi C_A (h^k)^2$, where C_A is another empirical coefficient. The force on each link is [14]

$$\mathbf{F}_A^k = -\mu_N^k \ddot{\mathbf{x}}^k \cdot \hat{\mathbf{n}}^k.$$

We now have the forces acting on each link fully defined, but still need to determine the corresponding fluid forces on the nodes. This is done by simply applying half of the fluid force from each link to each of its adjacent nodes [15], i.e.,

$$\mathbf{F}_{A,k} = \frac{1}{2}(\mathbf{F}_A^{k-1} + \mathbf{F}_A^k) \quad \text{and} \quad \mathbf{F}_{D,k} = \frac{1}{2}(\mathbf{F}_D^{k-1} + \mathbf{F}_D^k).$$

Note that this applies to internal nodes, which share two adjacent links, whereas the end nodes receive force contributions from only a single adjacent link.

IV. Control and Results

So far, we have presented a method for approximating the dynamics of free-swimming fish interacting with each other's wakes using a low-dimensional, closed-form model. This approach allows users to study flow interactions between fish over time without relying on full computational fluid dynamics (CFD) simulations. Notably, it also enables rapid design and testing of feedback control laws. The framework is particularly well-suited for tasks such as parameter tuning or training data-driven controllers that require running a large number of simulations efficiently. With this goal in mind, we now introduce a heading control law and simulate both single and multiple fish interactions, with and without control.

A. Controller Design

We introduce heading control through the wave bias term, ϕ_0 from (9). This bias term creates an asymmetric swimming pattern that causes the swimmer to turn left when $\phi_0 < 0$ and right when $\phi_0 > 0$. The controller includes a feedback term based on the current heading error, $h - h_{des}$, and a feedforward term, τ, which is the hydrodynamic drag the fish experiences due to the relative flow. The control law is

$$\phi_0 = 0.5 \tanh\left(\tau + 2[h - h_{des}]\right). \tag{17}$$

The feedforward term τ captures the influence of the flow on the heading and leads to a significant improvement over pure feedback control. While we do not model sensor outputs, prior work has proven the ability to sense the feedforward term using distributed pressure sensors along the fish body [26]; an IMU could be used to sense the feedback term $h - h_{des}$. The hyperbolic tangent function provides a smooth way to impose saturation limits and prevent the fish from bending over itself.

Fig. 5: Reference fish body positions over a full tail beat with $\phi_0 = -0.5$ (left), $\phi_0 = 0.0$ (middle), and $\phi_0 = 0.5$ (right).

B. Simulation Results

This section first presents the output of a single swimmer, both with and without control, as a benchmark before examining multi-fish interactions. Note that in all simulations, each fish flaps with a frequency of one full tail beat per second. The top subplot of Figure 6 shows the trajectory of a single fish swimming in the negative x-direction while shedding vortices with no steering applied. As expected, the swimmer exhibits fairly steady forward motion with slight drift caused by the influence of its own wake. The bottom subplot of Figure 6 shows the same swimmer using feedback to change its heading by $45°$ to the right and successfully maintain it.

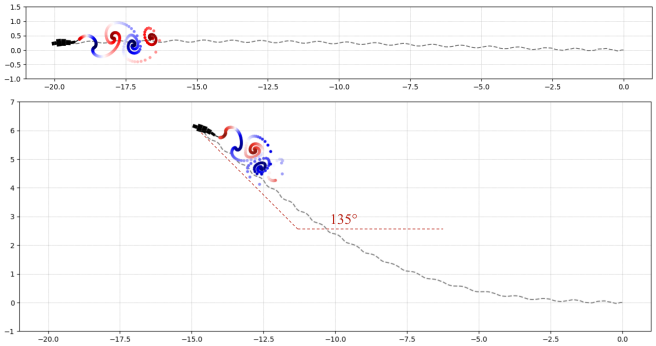

Fig. 6: Simulation of a single fish swimming without (top) and with (bottom) heading feedback control. Feedback controller drives fish from initial heading of $180°$ to a heading of $135°$. Discretized free vortex sheet strength indicated by red ($\Gamma > 0$) and blue ($\Gamma < 0$) dots. Trajectory over 20 seconds indicated by gray dashed line.

We next run simulations of two fish swimming side-by-side for 20 seconds, as shown in Figure 7. The top subplot shows the swimmers without control, where interactions with each other's wakes cause them to drift from their initial trajectories. In contrast, in the bottom subplot, which shows trajectories with steering control, we see that the fish experience some drift, but they are able to maintain a generally straight path and stay relatively close to one another.

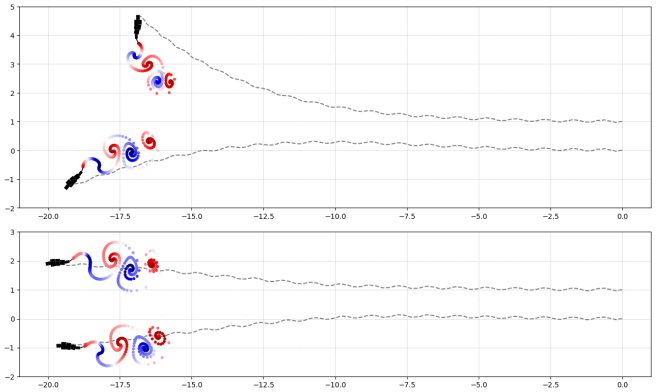

Fig. 7: Two fish without (top) and with (bottom) control to maintain 180° heading over 20 seconds. Fish initially have one fish length of lateral separation.

The final simulation shows a school of four fish arranged in a diamond formation using steering control to maintain forward motion. This configuration is well known to improve efficiency through hydrodynamic interactions [27]. The control strategy prevents the fish from turning and drifting off due to wake interactions. Additionally, the simulation successfully demonstrates the platform's ability to model typical schooling patterns, providing a foundation for future studies of such formations. Note that all simulations shown were run on a conventional computer without high-performance computing resources in under 20 minutes.

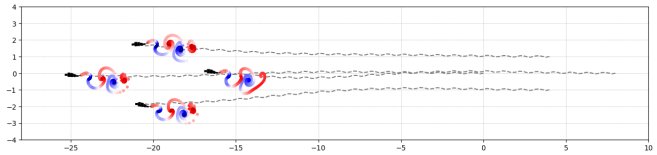

Fig. 8: Four fish in a diamond formation swimming in-phase with control to maintain 180° heading over 25 seconds.

V. Conclusion

We have introduced a framework for modeling interactions between multiple planar flexible fish swimming in close proximity within a fluid. We include a detailed explanation of the underlying theory for both the elastic body forcing model and the vortex sheet method, as well as the resulting hydrodynamic forces. We conclude the paper by demonstrating the method through simulations of single and multiple fish in various configurations, both with and without control. Ongoing work includes incorporating visual and hydrodynamic sensing to the platform for state estimation and validating outputs against benchmark CFD results.

References

[1] M. Sfakiotakis, D. M. Lane, and J. B. C. Davies, "Review of fish swimming modes for aquatic locomotion," *IEEE Journal of Oceanic Engineering*, vol. 24, no. 2, pp. 237–252, 1999.

[2] M. S. Triantafyllou, G. S. Triantafyllou, and D. K. P. Yue, "Hydrodynamics of fishlike swimming," *Annual Review of Fluid Mechanics*, vol. 32, p. 33–53, Jan. 2000.

[3] D. Weihs, "Hydromechanics of fish schooling," *Nature*, vol. 241, p. 290–291, Jan. 1973.

[4] J. C. Liao, D. N. Beal, G. V. Lauder, and M. S. Triantafyllou, "Fish exploiting vortices decrease muscle activity," *Science*, vol. 302, p. 1566–1569, Nov. 2003.

[5] J. C. Liao and O. Akanyeti, "Fish swimming in a kármán vortex street: Kinematics, sensory biology and energetics," *Marine Technology Society Journal*, vol. 51, p. 48–55, Sept. 2017.

[6] L. Li, M. Nagy, J. M. Graving, J. Bak-Coleman, G. Xie, and I. D. Couzin, "Vortex phase matching as a strategy for schooling in robots and in fish," *Nature Communications*, vol. 11, no. 1, p. 5408, 2020.

[7] S. Heydari, H. Hang, and E. Kanso, "Mapping spatial patterns to energetic benefits in groups of flow-coupled swimmers," *Elife*, pp. 2024–02, 2024.

[8] P. A. Dewey, B. M. Boschitsch, K. W. Moored, H. A. Stone, and A. J. Smits, "Scaling laws for the thrust production of flexible pitching panels," *Journal of Fluid Mechanics*, vol. 732, p. 29–46, Aug. 2013.

[9] D. Quinn and G. Lauder, "Tunable stiffness in fish robotics: mechanisms and advantages," *Bioinspiration & Biomimetics*, vol. 17, p. 011002, Dec. 2021.

[10] H. Hang, S. Heydari, J. H. Costello, and E. Kanso, "Active tail flexion in concert with passive hydrodynamic forces improves swimming speed and efficiency," *Journal of Fluid Mechanics*, vol. 932, p. A35, 2022.

[11] M. Bergou, M. Wardetzky, S. Robinson, B. Audoly, and E. Grinspun, "Discrete elastic rods," *ACM Transactions on Graphics*, vol. 27, pp. 1–12, 8 2008.

[12] M. K. Jawed, A. Novelia, and O. M. O'Reilly, *A primer on the kinematics of discrete elastic rods*. Cham, Switzerland: Springer International Publishing, 1 ed., May 2018.

[13] N. N. Goldberg, X. Huang, C. Majidi, A. Novelia, O. M. O'Reilly, D. A. Paley, and W. L. Scott, "On planar discrete elastic rod models for the locomotion of soft robots," *Soft Robotics*, vol. 6, pp. 595–610, 10 2019.

[14] E. Kelasidi, K. Y. Pettersen, J. T. Gravdahl, S. Stromsoyen, and A. Sorensen, "Modeling and propulsion methods of underwater snake robots," in *IEEE Conference on Control Technology and Applications*, pp. 819–826, IEEE, 8 2017.

[15] W. L. Scott, P. J. Prakash, and D. A. Paley, *Distributed Control of a Planar Discrete Elastic Rod for Eel-Inspired Underwater Locomotion*, pp. 261–279. Springer International Publishing, 2021.

[16] M. Nitsche and R. Krasny, "A numerical study of vortex ring formation at the edge of a circular tube," *Journal of Fluid Mechanics*, vol. 276, pp. 139–161, 1994.

[17] S. Ramananarivo, F. Fang, A. Oza, J. Zhang, and L. Ristroph, "Flow interactions lead to orderly formations of flapping wings in forward flight," *Physical Review Fluids*, vol. 1, no. 7, p. 071201, 2016.

[18] Y. Huang, M. Nitsche, and E. Kanso, "Hovering in oscillatory flows," *Journal of Fluid Mechanics*, vol. 804, pp. 531–549, 2016.

[19] Y. Huang, L. Ristroph, M. Luhar, and E. Kanso, "Bistability in the rotational motion of rigid and flexible flyers," *Journal of Fluid Mechanics*, vol. 849, pp. 1043–1067, 2018.

[20] S. Heydari and E. Kanso, "School cohesion, speed and efficiency are modulated by the swimmers flapping motion," *Journal of Fluid Mechanics*, vol. 922, 2021.

[21] W.-K. Yen and D. A. Paley, "Modeling inline oscillating foils using periodic conformal mapping," *Applied Ocean Research*, vol. 156, p. 104459, 2025.

[22] H. Xiong, *Geometric mechanics, ideal hydrodynamics, and the locomotion of planar shape-changing aquatic vehicles*. PhD thesis, University of Illinois Urbana-Champaign, 2007.

[23] K. Streitlien and M. S. Triantafyllou, "Force and moment on a Joukowski profile in the presence of point vortices," *AIAA Journal*, vol. 33, p. 603–610, Apr. 1995.

[24] S. Gupta, A. Agrawal, K. Hourigan, M. C. Thompson, and A. Sharma, "Anguilliform and carangiform fish-inspired hydrodynamic study for an undulating hydrofoil: Effect of shape and adaptive kinematics," *Physical Review Fluids*, vol. 7, p. 094102, 9 2022.

[25] M. A. Jones, "The separated flow of an inviscid fluid around a moving flat plate," *Journal of Fluid Mechanics*, vol. 496, pp. 405–441, 2003.

[26] Y. Xu and K. Mohseni, "Bioinspired hydrodynamic force feedforward for autonomous underwater vehicle control," *IEEE/ASME Transactions on Mechatronics*, vol. 19, no. 4, pp. 1127–1137, 2014.

[27] A. Menzer, Y. Pan, G. V. Lauder, and H. Dong, "Fish schools in a vertical diamond formation: Effect of vertical spacing on hydrodynamic interactions," *Physical Review Fluids*, vol. 10, Apr. 2025.